Research Article

Anand Vyas*, Ahmed Aliyu, and Gary Chi-Pong Tsui

Impact of carbon content on the phase structure and mechanical properties of TiBCN coatings *via* direct current magnetron sputtering

Abstract: In this study, unbalanced direct current magnetron sputtering was employed to develop TiBCN coatings on Si (100) wafers. The carbon (C) concentration was varied to manipulate the phase structure and mechanical properties of the coatings. The coatings were analyzed using Raman spectroscopy, scanning electron microscopy, X-ray diffraction, X-ray photoelectron spectroscopy, and nanoindentation. The results revealed that the TiBCN-2 coating, with a C concentration of 4.4 at.%, exhibited optimal hardness and elastic modulus values of 33 and 291 GPa, respectively. On the other hand, as the C content increased from 4.4 to 24.4 at.%, the hardness and elastic modulus values of the coatings decreased to 21 and 225 GPa, respectively, due to the formation of boron nitride and carbon phases within the coating matrix. Therefore, the inclusion of an ideal C concentration can considerably improve the properties of TiBCN coatings, thus rendering the coating a desirable material for cutting tools.

Keywords: magnetron sputtering, TiBCN coatings, Si (100) wafer substrate, microstructure, mechanical properties

1 Introduction

The engineering sector has grown quickly, resulting in an increase in the number of machine parts that can operate under various circumstances. Coatings that are based on borides, carbides, and nitrides, specifically TiB, TiC, TiN, TiB2, TiBC, TiCN, TiBN, and TiBCN, are of great importance in determining the functional properties of machining tools [1–3]. These coatings are carefully selected to optimize performance and longevity of the tool. For cutting tools, the T(C, N) ceramic component in cermet is particularly valuable due to its high refractoriness, wear and corrosion resistance, hardness, edge strength, edge sharpness, low density, and conductivity [4–9]. Similar to this, Ti(C, N)-based cermet is also utilized in automotive parts, bearings, and gas turbine components [10]. TiB_2 ultra-high temperature ceramic is used for high-temperature structural components due to its high specific strength and endurance [11,12]. Research has shown that combining TiB_2 and Ti (CN) compounds in ceramic composites can be used for a variety of applications due to their superior mechanical capabilities to those of individual ceramic components [13–16]. Other comparable nanocomposite hard coating systems that combine improved hardness, toughness, and reduced coefficient of friction have proven to be significant [3,17]. These systems, such as TiB, TiC, TiN, and TiB_2 compounds, do this by adding various materials gradually and intelligently to a hard single-component phase.

To further enhance the quality of these ceramic compounds, a novel and intriguing material based on the TiBCN composite has been developed [2]. As in the Ti(C, N) ceramic phase [2,18], these nanocomposites exhibit a face-centered cubic structure, where boron (B) is positioned in the same crystallographic position as carbon (C) and nitrogen (N). The unique properties of the TiBCN composite are mostly based on solid solution hardening. It is envisaged that nanometric TiCN and TiB_2 would embed during this solid solution hardening process as amorphous boron nitride (BN) and carbon matrix are formed. The change in the C contents within the coating matrix is anticipated to significantly influence the phase structure and mechanical properties of TiBCN coatings. In order to correlate the structure of the phase with the mechanical properties of the resulting TiBCN coatings, the current work

---

* **Corresponding author: Anand Vyas**, Division of Science, Engineering and Health Studies, SPEED, The Hong Kong Polytechnic University, Hong Kong, China, e-mail: anand.vyas@cpce-polyu.edu.hk, tel: +852-37460350

Ahmed Aliyu: Department of Chemical Engineering, Federal University Wukari, Wukari, Taraba State, Nigeria; Department of Materials Engineering, Indian Institute of Science, Bangalore, India

Gary Chi-Pong Tsui: State Key Laboratory of Ultra-precision Machining Technology, Department of Industrial and System Engineering, The Hong Kong Polytechnic University, Hong Kong, China

aims to investigate the effect of C concentration (ranging from 0.0 to 24.4 at.%) in an unbalanced direct current (DC) magnetron sputtering of TiBCN coatings onto Si (100) substrates. Raman spectroscopy, X-ray diffraction (XRD), X-ray photoelectron spectroscopy (XPS), and optical microscopy methods were used to investigate the phase structure of the TiBCN coatings. However, the nanoindentation method was used to determine the mechanical properties.

2 Experiment

2.1 TiBCN coating deposition on wafers

Thin films of TiBCN were deposited onto Si(100) substrates using unbalanced DC-magnetron sputtering equipment (UDP450, Teer Coating Limited). The deposition process involved the use of one Ti, one TiB_2, and two C targets. To achieve coatings with different carbon content, the C target current was varied from 0.0 to 2.0 A, while the Ti target current and TiB_2 target current were held constant at 6.0 and 3.0 A, respectively. The process enabled the deposition of TiBCN coatings that differed in their carbon content. The coatings were designated as TiBCN-1 (0 at.% C), TiBCN-2 (4.4 at.% C), TiBCN-3 (12.4 at.% C), TiBCN-4 (19.2 at.% C), and TiBCN-5 (24.4 at.% C). The substrate rotation speed was maintained at 15 rpm, while the substrate bias voltage was −60 V. The process was carried out under an operating pressure of 0.26 Pa, and the amount of nitrogen added to the chamber was measured using a computer-controlled optical emission spectroscopy instrument set at 80%.

Prior to the deposition, the surface of the substrate was maintained at a negative bias voltage of 500 V for 30 min with Ar plasma. Next, a Ti buffer layer of 100 nm in thickness was deposited. The objective of depositing this Ti buffer layer was to not only increase the coating adhesion but also decrease the stress at the interface with the Si (100) substrate. Due to plasma heating, the substrate temperature was estimated to be around 200°C during deposition. The schematic diagram depicting the experimental set-up, followed by the characterization technique, is presented in Figure 1.

2.2 Characterization

X-ray photoelectron spectroscopy (XPS, PHI 5802 system) with a monochromatic Al Kα X-ray source (h = 1486.6 eV) was used to investigate elemental concentration and the bonding status in the coatings. The surface morphology and composition of the coatings were analyzed using the scanning electron microscope (ESEM Quanta 200 SEM) equipped with an energy-dispersive X-ray spectroscopy (EDS) detector at 25 kV. LABRAM HR-800 Raman spectroscope was used to examine the chemical substance and structure of the coatings. Using a Rigaku MiniFlex diffractometer, operating at 40 kV and 30 mA, XRD was used to determine the crystalline structure of the coatings. Cu Kα radiation was used for the experiments, and an Ni filter was used to cut off Cu Kα reflections. Using a trigonal Berkovich diamond tip indenter with a maximum load of 1,000 mN, nanoindentation studies were used to determine
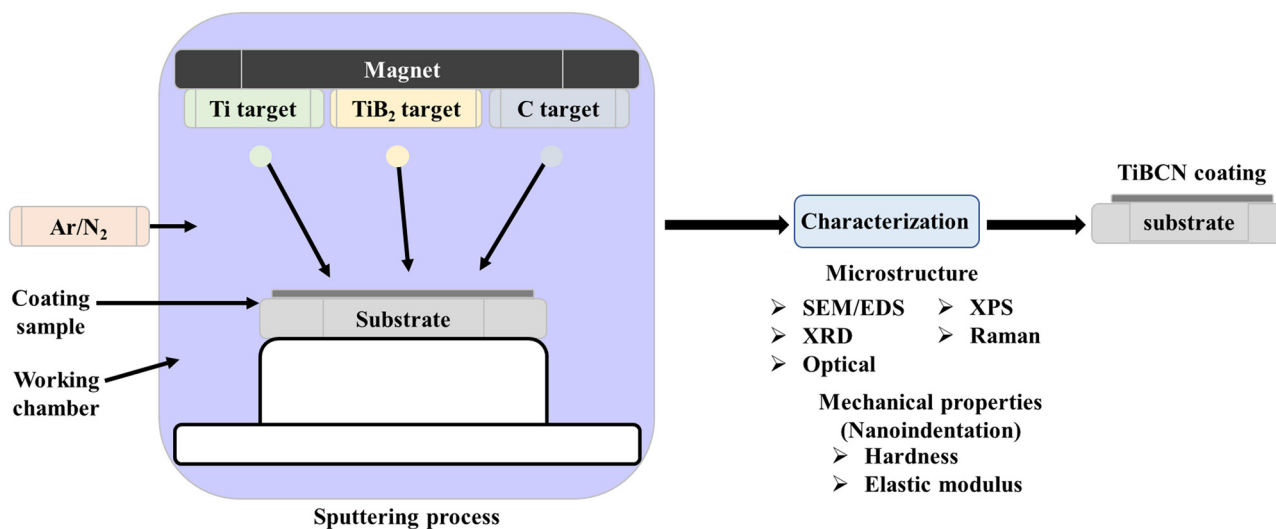

Figure 1: Schematic diagram of DC magnetron sputtering deposition of TiBCN coatings.

the elastic modulus and nano-hardness. For calibration reasons, the hardness value of a fused silica sample was routinely verified. Ten different measurements were made for each sample to calculate the mean. By employing a Teer 3001 scratch tester, the cohesive and adhesive strengths of the coatings were evaluated. A diamond indenter with a 0.2 mm radius was moved across the coatings at a sliding velocity of 10 nm·min^{-1} and a loading rate of 100 N·min^{-1}.

3 Results and discussion

Figure 2 displays the elemental concentration of TiBCN coatings (atomic percentage (at.%)). According to Figure 2, the C concentration increases linearly as the C target current increases from 0.0 to 2.0 A, whereas the Ti and N atomic concentrations within the coating matrix show the reverse trend. It was determined that B's atomic concentration in the coating matrix is between 10.5 and 14.4 at.%. The observed differences in the concentration of the elements in Figure 2 can be attributed to the various phase formations within the coatings matrix, as detailed later in the Raman and XRD results, which may have an impact on the mechanical properties of the coatings. Figure 3 shows the observed scanning electron microscopy (SEM) images of the cross-sectional morphology of the TiBCN coatings. According to the cross-section SEM images of the TiBCN film, the overall coating thickness is around ~1 μm for all coating conditions, with the exception of TiBCN-5, which shows a thickness of 0.68 μm. Additionally,
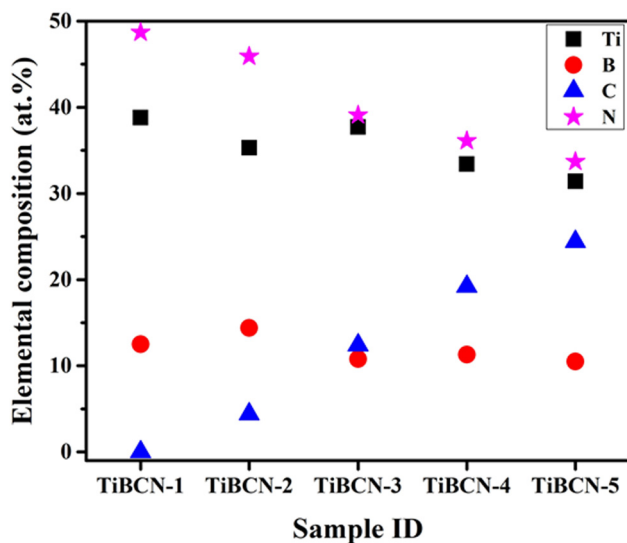
the cross-sectional view of the coatings appears to be uniform across all coatings conditions.

The Raman spectra were obtained to compare the C–C bonding structure present in different TiBCN coatings. The coatings were tested at varying C concentrations, ranging from 0 to 24.4 at.% in the wave range of 1,000–2,000 cm^{-1} (as shown in Figures 4 and 5). The inset figures in Figure 4 illustrate the spectra fitting using the Gaussian function to determine the peak area and the full-width half maximum (FWHM). The G peak, representing sp^2-C (sp^2-bond), and the D peaks, representing sp^3-C (sp^3-bond), are depicted

Figure 3: SEM cross-sectional images of TiBCN coatings at different C concentrations.
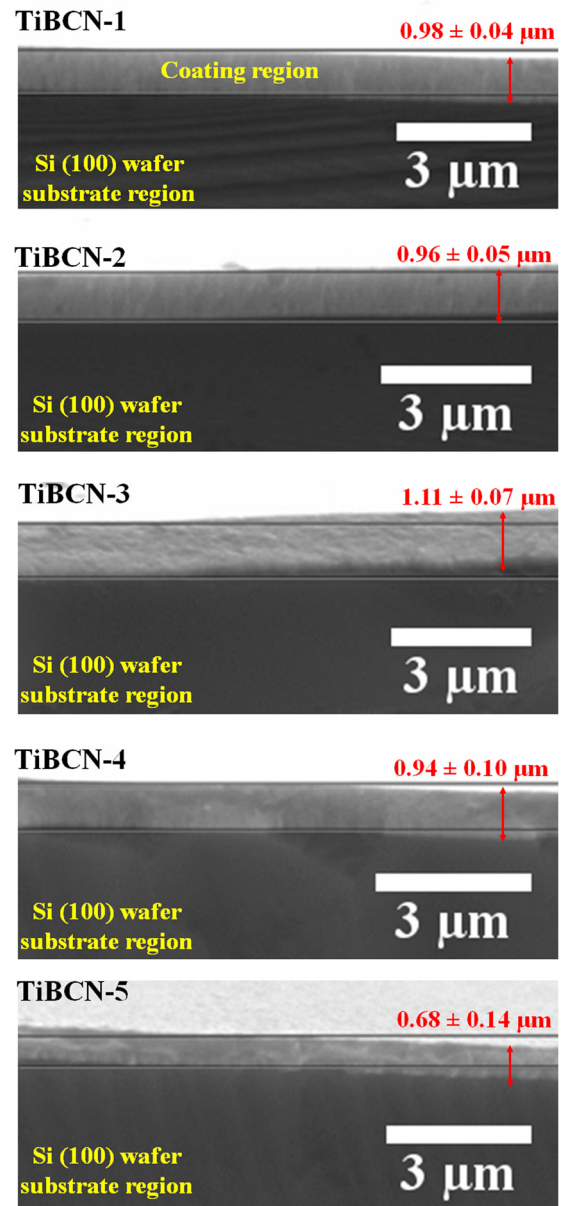

Figure 2: Elemental composition of TiBCN coatings at different C concentrations.

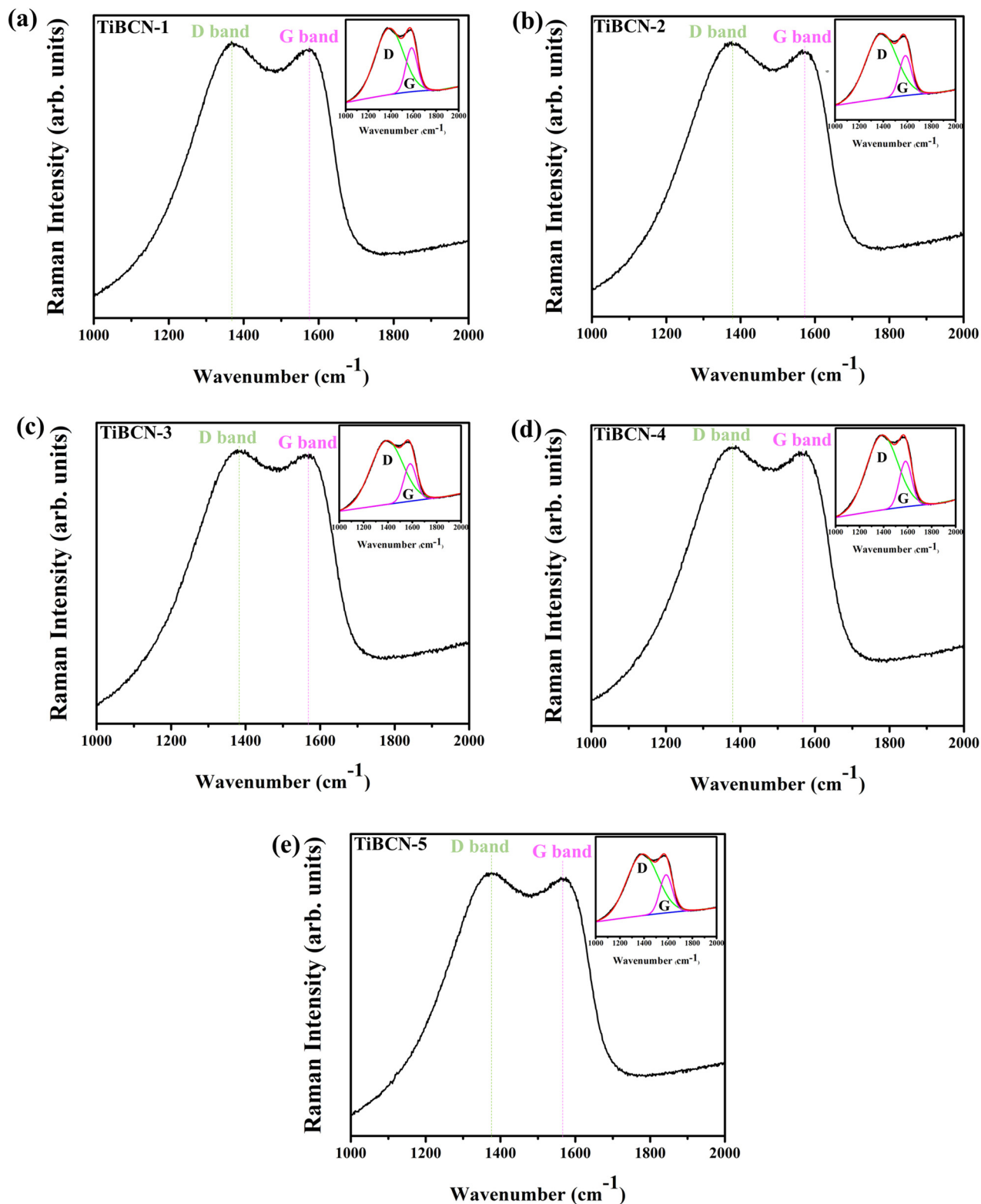**Figure 4:** Raman spectra of TiBCN coatings at (a) 0 at.% C, (b) 4.4 at.% C, (c) 12.4 at.% C, (d) 19.2 at.% C, and (e) 24.4 at.% C concentration.
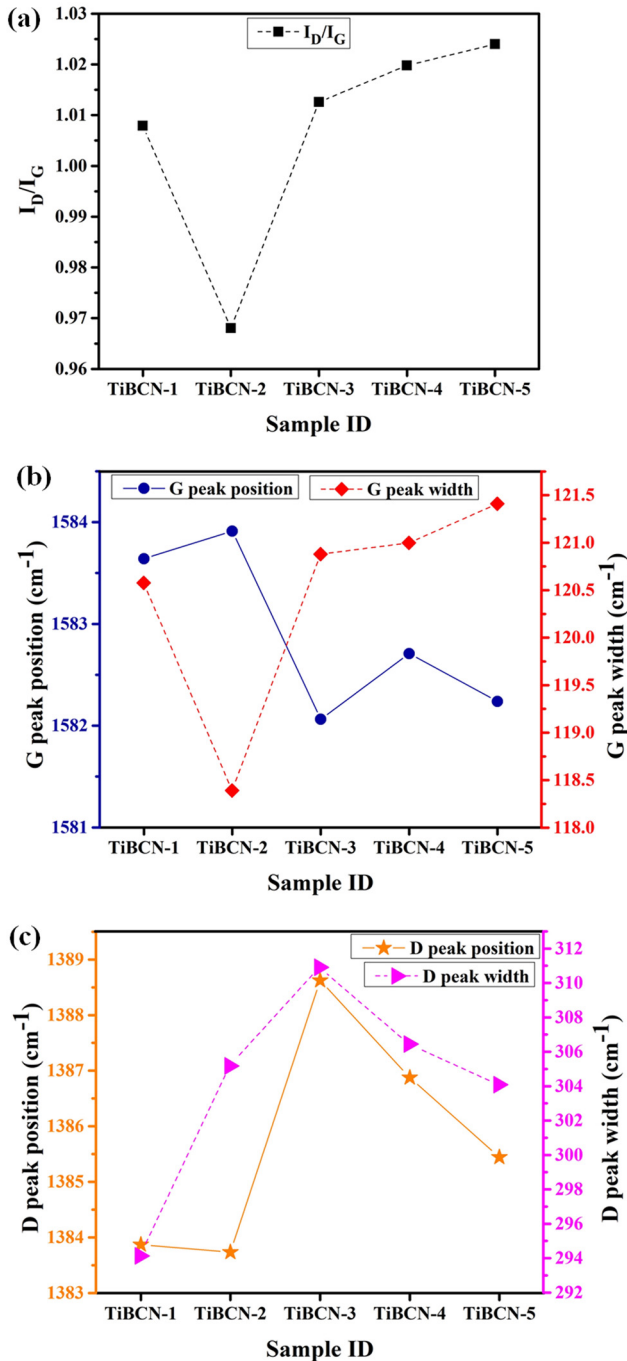
(a)

(b)

(c)

Figure 5: Raman parameters determined by Gaussian curve-fitting of TiBCN coatings (a) I_D/I_G ratio, (b) G peak position and width, and (c) D peak position and width.
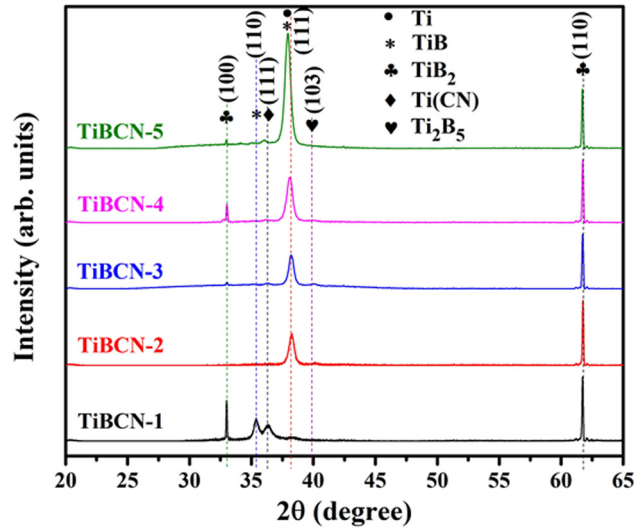

Figure 6: XRD patterns of TiBCN coatings at different C concentrations.

prevent the formation of a graphite-like structure. As the C concentration increases from 4.4 to 24.4 at.%, the ratio increases to 1.0240, indicating an increase in the sp^2-C concentration and the graphitic characteristics of the coatings after C incorporation. The position and peak width (FWHM) of the G and D peaks change with the C concentration, as shown in Figure 5(b) and (c). The G peak width (FWHM) measures the bond length and bond angle disorder in sp^2 clusters. The size and strain of the sp^2 clusters inside the sp^3 network increase as the sp^3 content decreases, leading to lower length and bond angle disorder and reducing G peak width [21]. As the C concentration increases in Figure 5(b), the G peak position shows only minor fluctuations in the limited range of 1583.64 to 1582.24 cm^{-1}, indicating a slight change in the coatings' sp^2 and sp^3 content. The little shift in the G peak width is similarly accompanied by an increase in the sp^2 contents in the 120.59–121.41 cm^{-1} range.

The XRD patterns of TiBCN coatings at various C concentrations are depicted in Figure 6. The TiBCN coating displayed an intensity peak at 32.99° that corresponds to a hexagonal TiB_2-type (100) at 0 at.% C. The orientation of the coating to TiB-type (111) after adding C to the film, along with the disappearance/low intensity of the TiB_2-type (100) and the coating's broadness, points to the possibility that the C in the coating matrix exists as either interstitial or substitutional atoms in the TiB_2 lattice [22]. It is important to note that both TiN and TiC possess NaCl structures in which, at the corners of the face center cubic structure, Ti atoms are distributed, whereas C or N atoms exist at the interstitial sites of the octahedron. Additionally, the Scherrer formula was used to determine the crystallite size of the TiBCN coatings [23]. The calculated crystallite sizes are
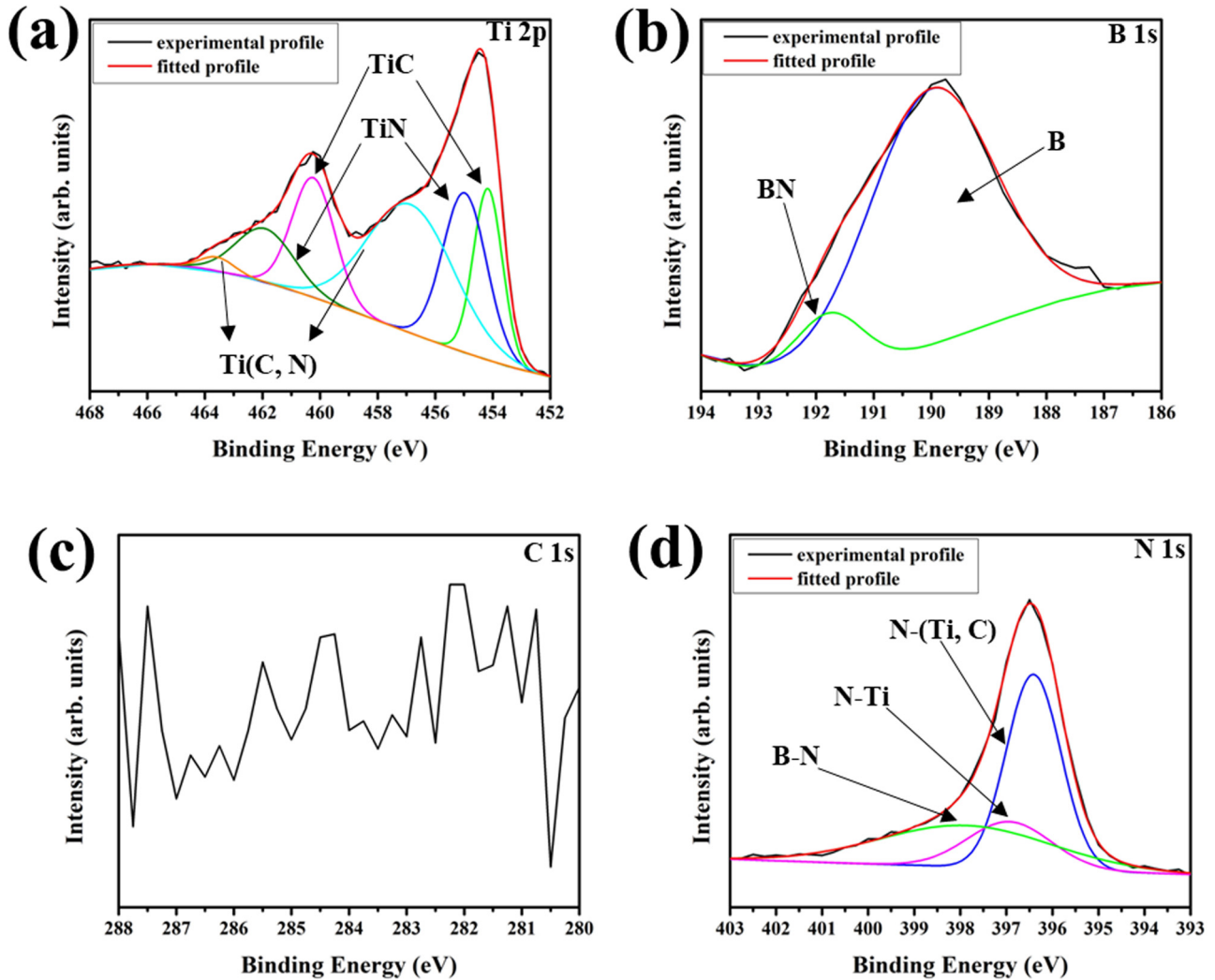
in Figure 5(a)–(e) at approximately 1,581 and 1,385 cm^{-1}, respectively [19,20]. Figure 5(a) illustrates the peak area ratio (I_D/I_G) as a function of the C target current, which represents the ratio of sp^3 and sp^2 in the coating. The I_D/I_G ratio falls from 1.0079 to 0.9681 as the C concentration increases from 0 to 4.4 at.%, indicating a minor increase in the sp^3 content due to the additional B and N atoms that

Figure 7: XPS spectra of (a) Ti 2p, (b) B 1s, (c) C 1s, and (d) N 1s energy regions of TiBCN-1 coatings at 0 at.% C concentrations.

39.70, 34.9, 27.5, 31.8, and 19.5 nm for the coating with C concentrations ranging from 0 to 24.4 at.%, respectively. This suggests that the inclusion of C into the TiBCN matrix will affect how the coating grows.

XPS was used to characterize the chemical binding states of the TiBCN coatings at various C concentrations between 0 and 24.4 at.%. Figure 7 displays the Ti 2p, B 1s, C 1s, and N 1s XPS core level spectra. The coatings showed identical Ti $2p_{3/2}$ and Ti $2p_{1/2}$ peaks in the Ti 2p spectra shown in Figures 7(a), 8(a), 9(a), 10(a) and 11(a) at energies of 454.5 and 460.25 eV, respectively. Due to the near binding energies of TiC (454.5/460.5 eV), TiN (455.5/462 eV), and Ti(C, N) (457/463.9), the Ti atoms might be bound to both B, C, and N atoms, as shown by these binding energies (*i.e.*, 454.5 and 460.25 eV) [24]. The Ti $2p_{3/2}$ and Ti $2p_{1/2}$ peaks gradually move towards the higher binding energy as the C content in the coatings rises, which is a sign of a

decline in the TiB and an increase in the TiN bonds in the coatings.

Figures 7(b), 8(b), 9(b), 10(b) and 11(b) B 1s spectra demonstrate the presence of B (189.3 eV) and BN (190.6 eV) bonding states. The intensity of the BN component inside the coatings matrix dramatically rises with an increase in the C contents. It is assumed that the BN phase in the coatings is in the amorphous condition because the XRD patterns showed no sign of crystalline h-BN. The N–(Ti, C) (396.7 eV), N–Ti (397.1 eV), and B–N (398.2 eV) bonding states made up the three primary species of the N 1s spectra in Figures 7(d), 8(d), 9(d), 10(d) and 11(d). As the coatings' C concentrations rise, the N–(Ti, C) component's intensity also rises.

The low C concentration in the TiBCN-1 coating is the reason why Figure 7(c) does not display a significant spectra component, but Figures 8(c), 9(c), 10(c) and 11(c)
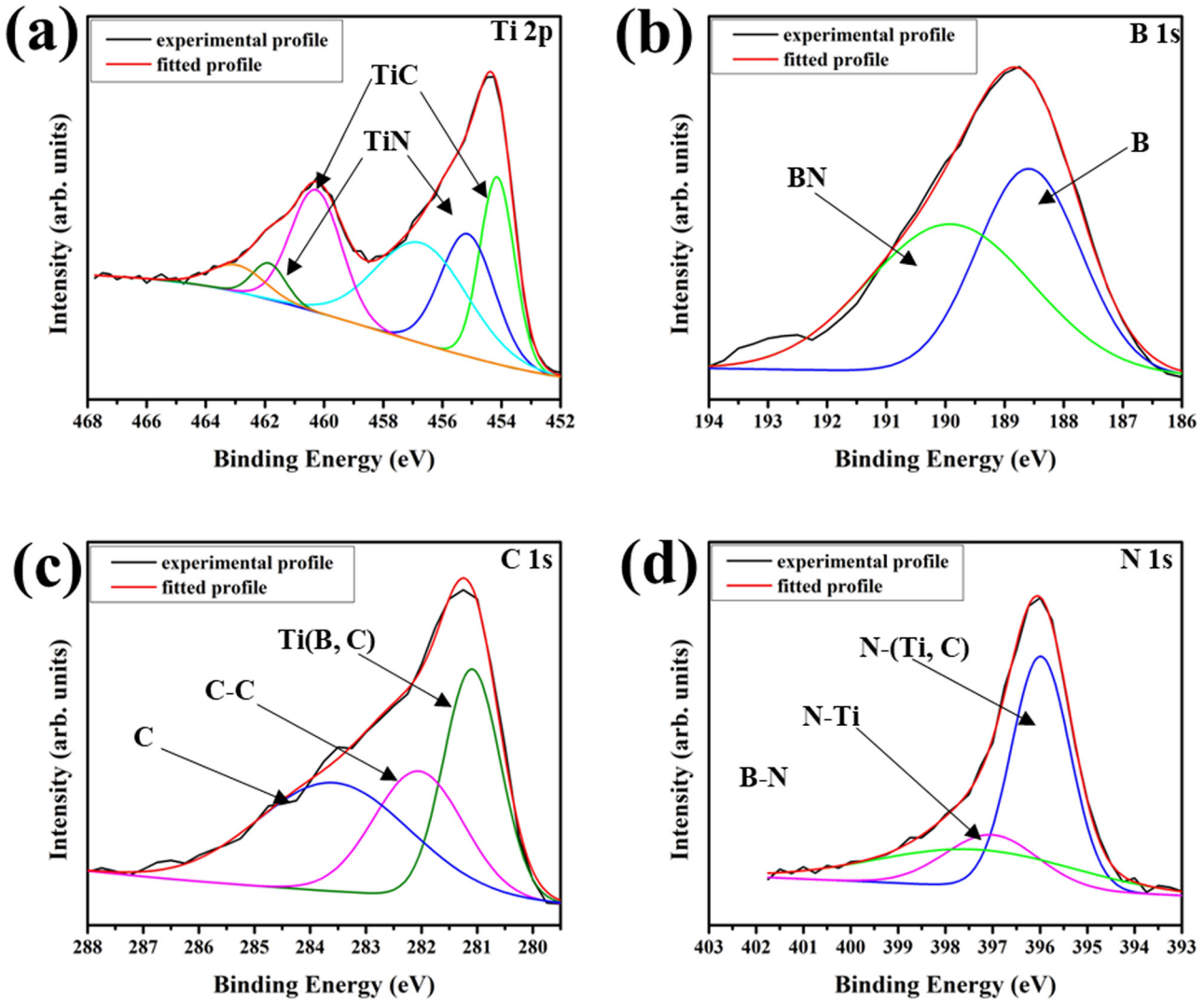
Figure 8: XPS spectra of Ti 2p, B 1s, C 1s, and N 1s energy regions of TiBCN-2 coatings at 4.4 at.% C concentrations.

all show three substantial components in the C 1s spectra at the binding energies of 281.5, 282, and 284 eV. The component at the binding energy 281.5 eV indicates the potential formation of a metal carbide in the form of Ti–(B, C), while the component at the binding energy 282.5 eV is attributed to the sp^2 amorphous C–C bonding and the component at the binding energy of 284 eV is a possible indication of the formation of the CN phase. Although a gradual chemical shift of the Ti–(B, C) peak with increasing C contents has been detected, this suggests that there were fewer B atoms linked to C atoms in the T–(B, C) solid solution.

Figure 12 displays the elastic modulus and hardness of TiBCN coatings with various C concentrations. When C with a concentration of 4.4 at.% is added, the hardness changes from 32 to 33 GPa, and the elastic modulus rises

from 279 to 291 GPa. The coating's hardness and elastic modulus drop to 21 and 225 GPa, respectively, as the C concentration is raised to 24.4 at.% in the coating. The observed alterations in the coating's phase structure, as determined by XRD (Figure 6), can be used to explain these changes. An indicator that the compressive stress and micro-hardness are decreasing, for instance, is a shift in the diffraction peak to a higher 2θ angle [20,25]. The production of an amorphous graphitic structure in the coatings is explained by the D and G peaks in the Raman spectra, but this structure can reduce the hardness of the coating due to its poor shear strength [1]. This study found that the TiBCN-2 coating's amorphous C content, particularly the sp^2 content, had decreased. This finding was supported by a decline in the I_D/I_G ratio from 1.0079 to 0.9681
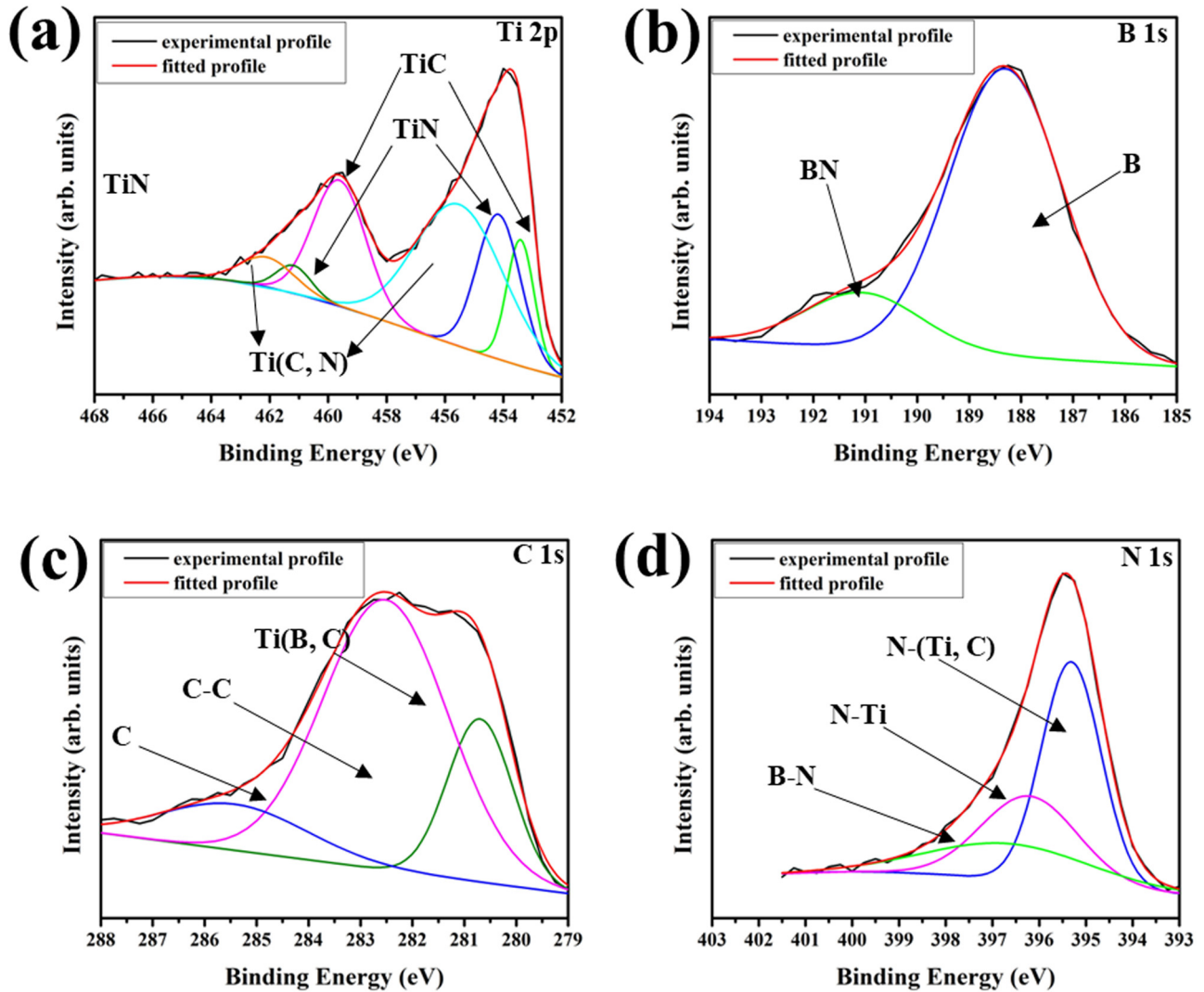
Figure 9: XPS spectra of Ti 2p, B 1s, C 1s, and N 1s energy regions of TiBCN-3 coatings at 12.4 at.% C concentrations.

(Figure 5(a)). The I_D/I_G ratio rises to 1.0240 when the C concentration rises from 4.4 to 24.4 at.%. Consequently, the elastic modulus and hardness both drop (Figure 12).

The cohesive and adhesive properties of the TiBCN coatings at different C concentrations were evaluated using scratch adhesion tests with increasing loads ranging from 10 to 80 N. Table 1 shows the calculated critical load values for cohesive (L_{C1}) and adhesive (L_{C2}) failure. The critical load is influenced by testing parameters used, like loading rate, indenter radius, scratching speed, coating thickness, friction coefficient, and residual stress [1]. The information on the frictional and plastic deformation of the coating system is contained in the friction coefficient (Ft/Fn). The critical loads were ascertained from the acquired friction plots (Friction [N] *versus* load [N]) shown in Figure 13 by examining the first and second onsets of significantly

abrupt fluctuation in the friction forces. The TiBCN-1 micrograph in Figure 12 shows chipping, conformal buckling, or interfacial spallation at a critical load, L_{C1} = 39 N (*i.e.*, C-free coating). Chipping results from a surface or internal crack. Furthermore, the second start of the increased frictional force curve that yields adhesive failure values comes at critical load L_{C2}, which is a point of inflection. The TiBCN-1 coating has an L_{C2} greater than 65 N. Additionally, the acoustic emission (AE) signal is used to determine the L_C values since the crack detected by the AE transducer produces an AE signal. All of the coating samples had distinct AE events that provided details on the extent of coating damage, which is shown in Figure 13. Critical load levels and frictional curves match up nicely. The outcome was identical, with L_{C1} equaling 42 N when the C concentration increased from 0 to 4.4 at.%. The
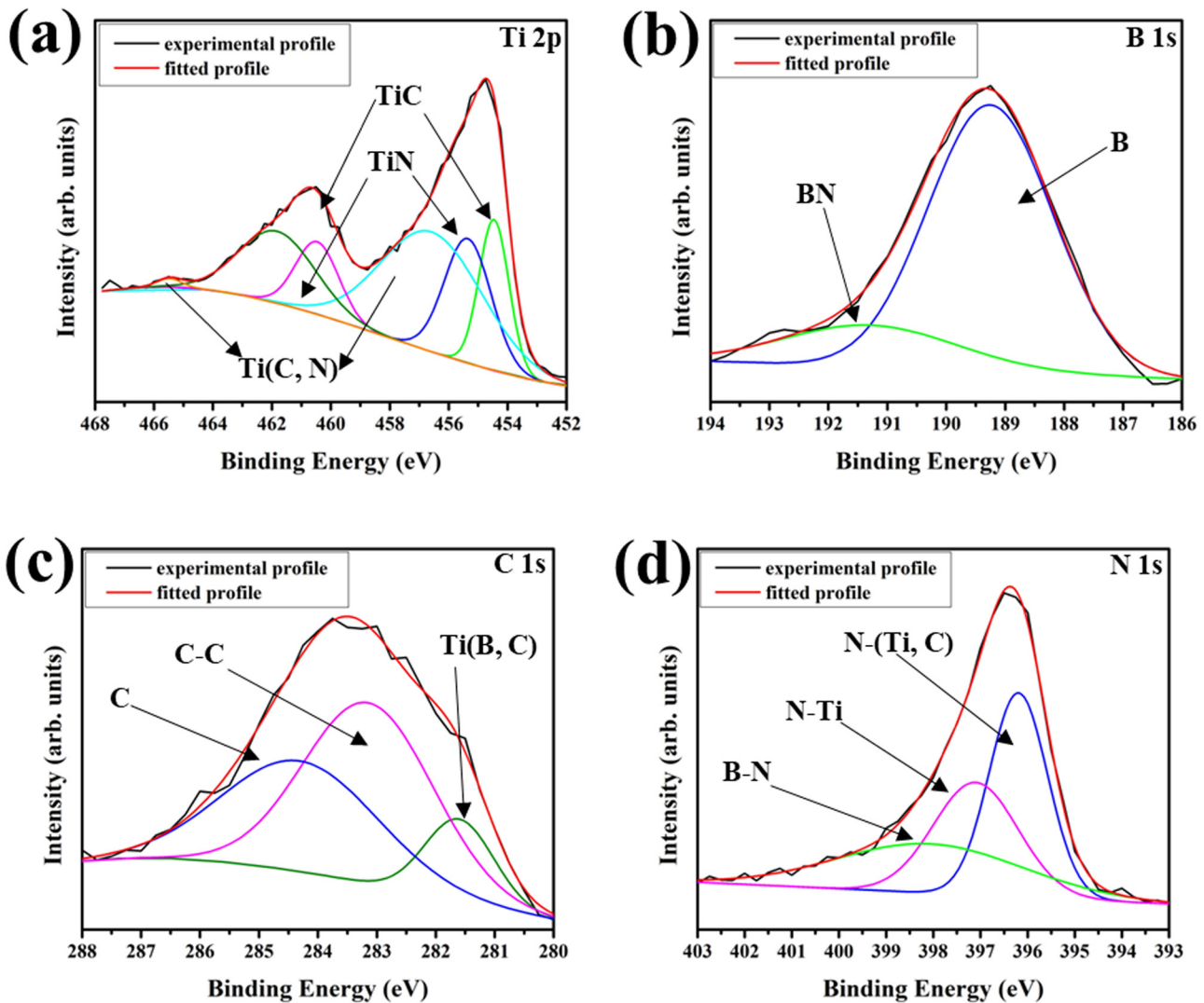
Figure 10: XPS spectra of Ti 2p, B 1s, C 1s, and N 1s energy regions of TiBCN-4 coatings at 19.2 at.% C concentrations.

beginning of cracking at the edges of the scratch track, which is plainly evident, is indicated by L_{C1} in accordance with the AE signal curves of TiBCN-3, TiBCN-4, and TiBCN-5 coatings.

However, the first abrupt rise of the acoustic signal cannot be used alone to understand the L_C values [1]. The straightforward acoustic signal is insufficient to assess the coating strength due to the intricacy of the contact and failure mechanism. As a result, all the coating samples were subjected to a scratch examination in order to assess the adhesion strength of coatings. The optical micrographs of all the TiBCN coating failure behaviors are displayed in Figure 14 as a result. However, when the C concentration increased, the scratch track underwent plastic deformation without spallation or chipping, as shown by the optical micrograph of TiBCN-3, TiBCN-4, and TiBCN-5 in Figure 14. The critical loads have been established and are shown in

Table 1 after accounting for the frictional plots, AE signal, and optical observations.

4 Conclusion

TiBCN coatings were deposited onto Si (100) wafer substrates using an unbalanced DC magnetron sputtering approach, with a range of C concentrations from 0 to 24.4 at.%. XRD analysis determined that the coatings contained crystalline phases of TiB_2/Ti(B, C), TN/Ti(C, N), and Ti_2B_5 within the amorphous phase of the coating matrix. XPS spectrum analysis showed the presence of Ti(B, C), Ti (C, N), TiN, BN, B–C, Ti–N, sp^2C–C, and sp^3C in the TiBCN coatings. Among the coatings, the TiBCN-2 (4.4 at.% C) demonstrated the optimal hardness and elastic modulus
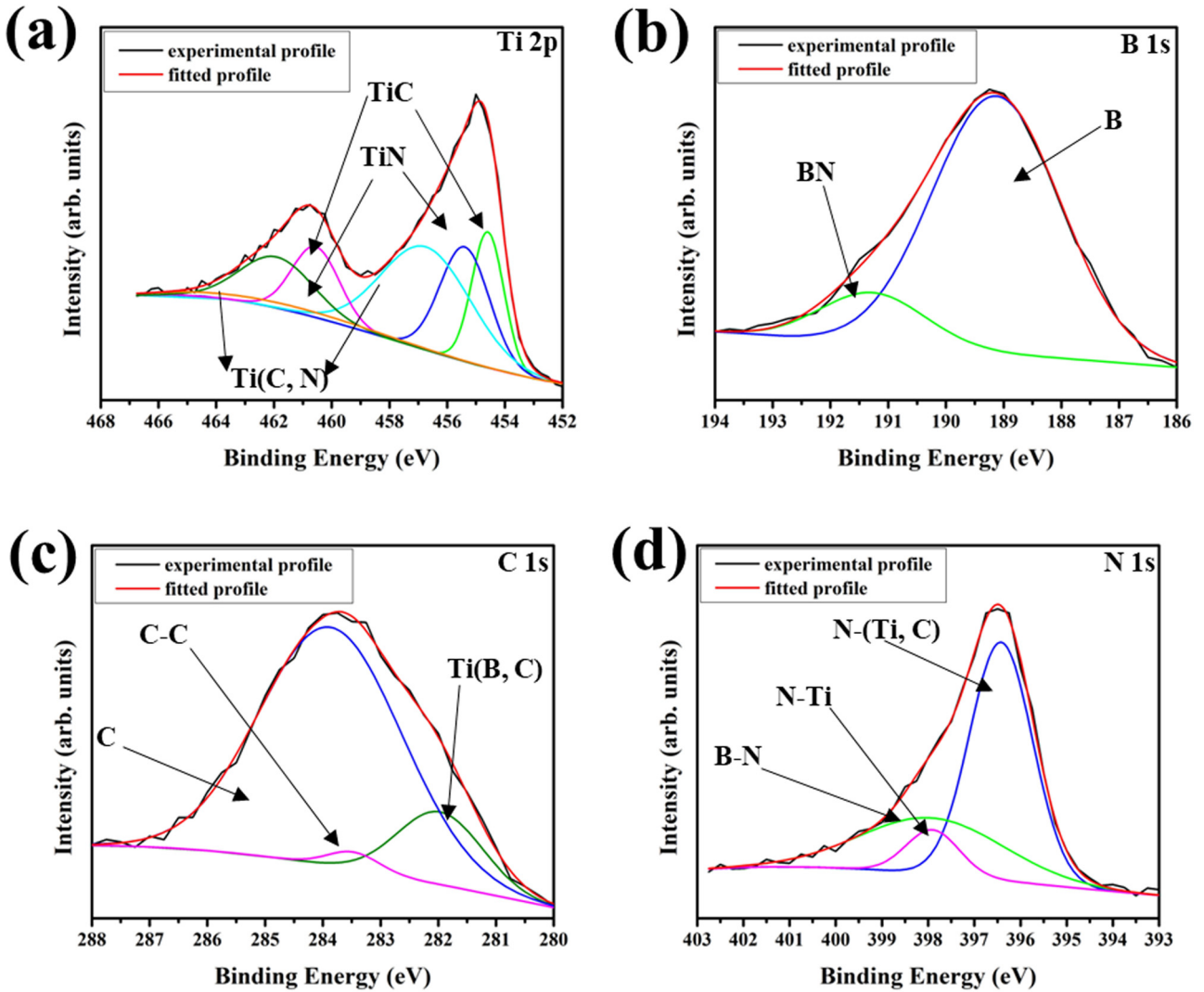
Figure 11: XPS spectra of Ti 2p, B 1s, C 1s, and N 1s energy regions of TiBCN-5 coatings at 24.4 at.% C concentrations.
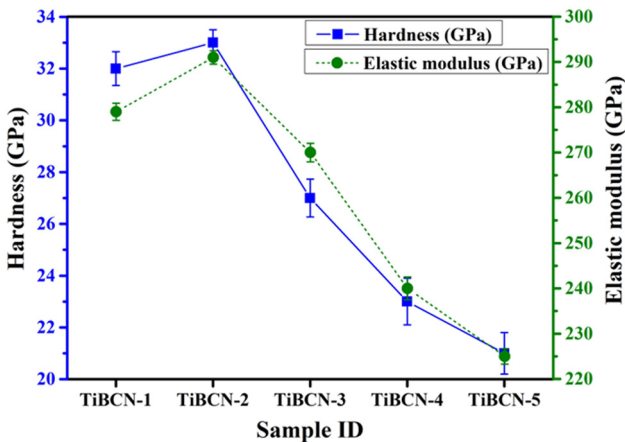

Figure 12: Hardness and elastic modulus of TiBCN coatings at different C concentrations.

Table 1: Scratch test measurements of TiBCN coatings with different C concentrations

Sample	TiBCN-1	TiBCN-2	TiBCN-3	TiBCN-4	TiBCN-5
$L_{C1}{}^a$ (N)	39	42	27	27	17
$L_{C2}{}^b$ (N)	>65	>75	>75	>75	>75

$L_{C1}{}^a$ (N) is the critical load for cohesive failure and defined as the load at which the coating shows first chipping on the scratch track. $L_{C2}{}^b$ (N) is the critical load for adhesive failure and defined as the load at which the substrate is showed on the scratch track.

of 33 and 291 GPa, respectively. As the C concentration increased in the TiBCN coatings, the nano-hardness and elastic modulus decreased. The increased nano-hardness and elastic modulus of the TiBCN-2 coatings were attributed
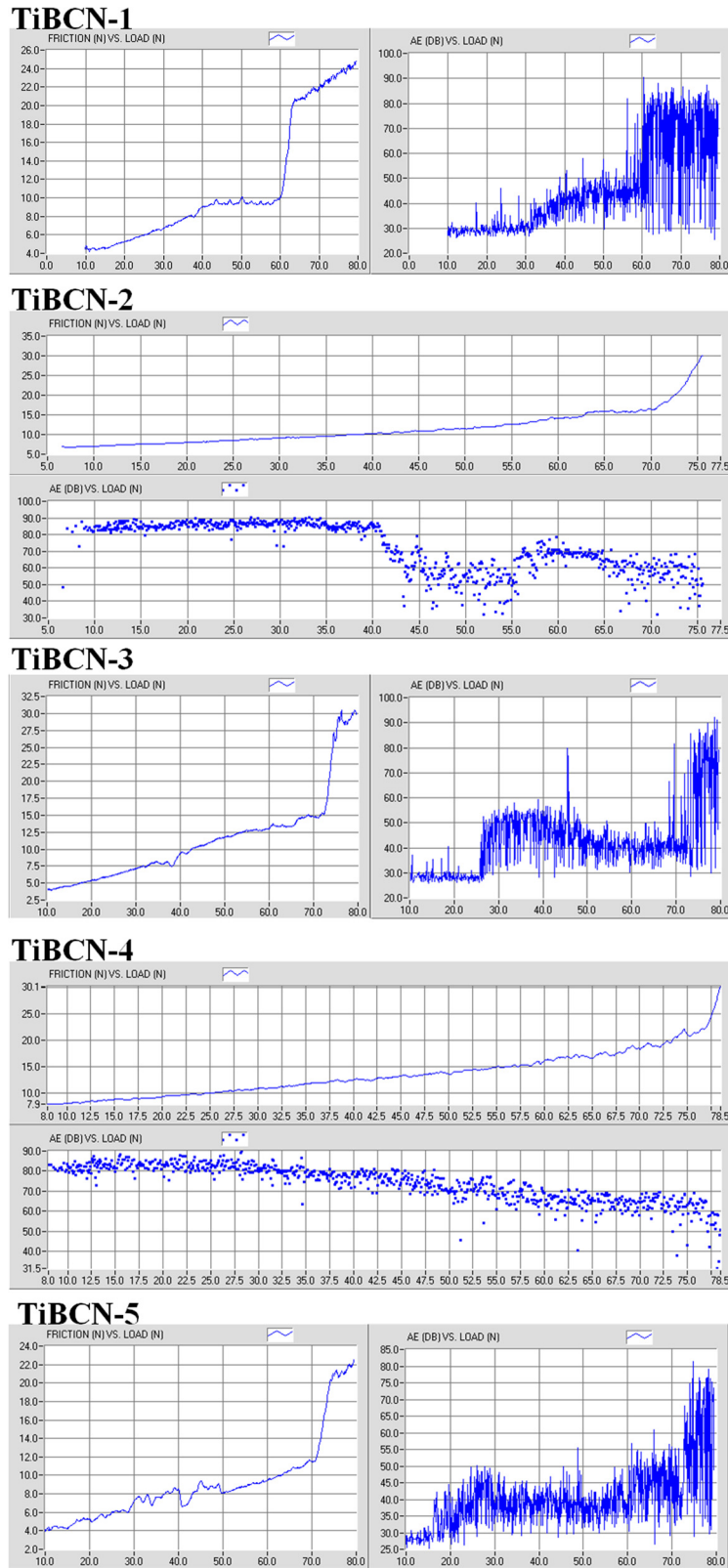
Figure 13: Frictional and AE signal *versus* load of TiBCN coatings at different C concentrations.
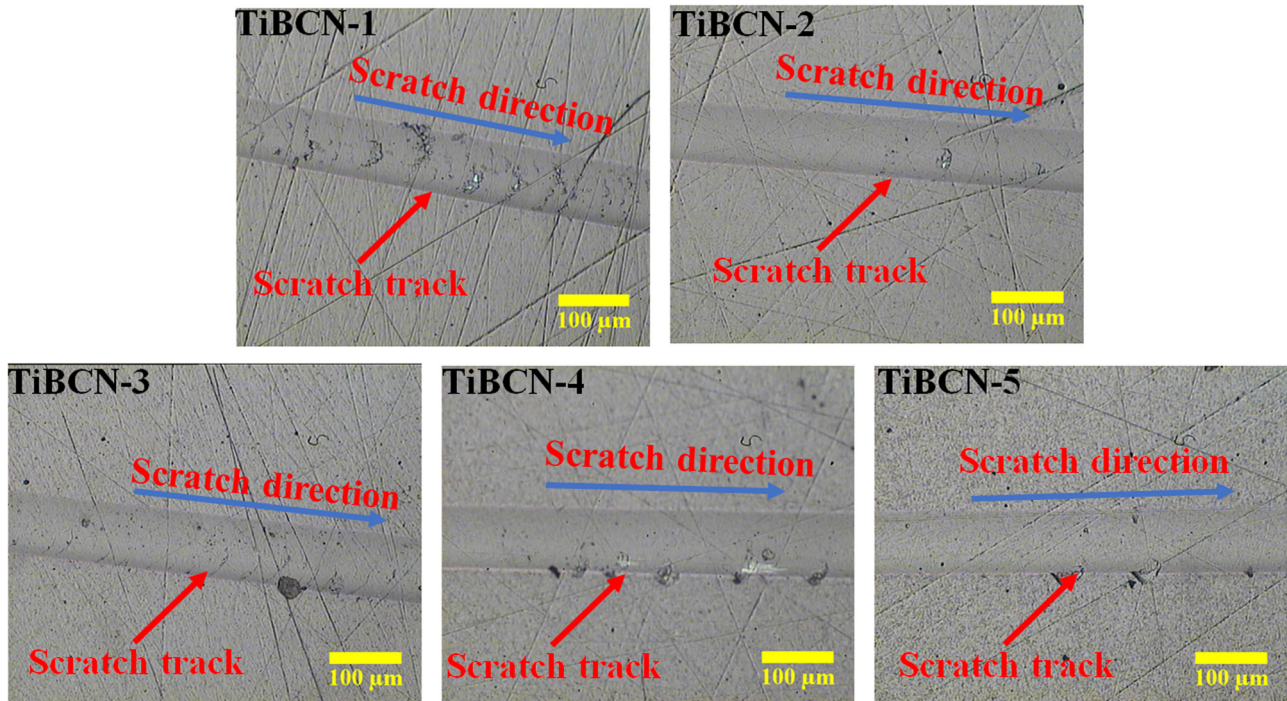
Figure 14: Optical micrographs displaying the scratch trails on TiBCN coatings at different C concentrations.

to the low amorphous phase fraction and declining sp^3/sp^2 ratio.

Author contributions: Anand Vyas: conceived and designed the experiments; performed the experiments; contributed reagents, materials, analysis tools, or data; wrote the article. Ahmed Aliyu: analyzed and interpreted the data; wrote the article. Gary Chi-Pong Tsui: analyzed and reviewed. All authors have accepted responsibility for the entire content of this manuscript and approved its submission.

Conflict of interest: The authors state no conflict of interest.

References

[1] Cheng, Y. H., T. Browne, B. Heckerman, and E. I. Meletis. Influence of the C content on the mechanical and tribological properties of the TiCN coatings deposited by LAFAD technique. *Surface and Coatings Technology*, Vol. 205, 2011, pp. 4024–4029.

[2] Lin, J. L., J. J. Moore, B. Mishra, M. Pinkas, and W. D. Sproul. The structure and mechanical and tribological properties of TiBCN nanocomposite coatings. *Acta Materialia*, Vol. 58, 2010, pp. 1554–1564.

[3] Mishra, S. K. Toughening of nanocomposite hard coatings. *Reviews on Advanced Materials Science*, Vol. 59, 2020, pp. 553–585.

[4] Zhang, H., J. Yan, X. Zhang, and S. Tang. Properties of titanium carbonitride matrix cermets. *International Journal of Refractory Metals and Hard Materials*, Vol. 24, 2006, pp. 236–239.

[5] Chicardi, E., J. M. Cordoba, and F. J. Gotor. High temperature oxidation resistance of (Ti, Ta)(C,N)-based cermets. *Corrosion Science*, Vol. 102, 2016, pp. 125–136.

[6] Zhang, S. Titanium carbonitride-based cermets: Processes and properties. *Materials Science & Engineering, A: Structural Materials: Properties, Microstructure and Processing*, Vol. 163, 1993, pp. 141–148.

[7] Li, Y., K. Su, P. Bar, L. Wu, H. Liu, H. Su, et al. Effect of TiBCN content on microstructure and properties of laser cladding Ti/TiBCN composite coatings. *Metals And Materials International*, Vol. 25, 2019, pp. 1366–1377.

[8] Levi, G., W. D. Kaplan, and M. Bamberger. Structure refinement of titanium carbonitride (TiCN). *Materials Letters*, Vol. 35, 1998, pp. 344–350.

[9] Angerer, P., L. G. Yu, K. A. Khor, G. Korb, and I. Zalite. Spark-plasma-sintering (SPS) of nanostructured titanium carbonitride powders. *Journal of the European Ceramic Society*, Vol. 25, 2005, pp. 1919–1927.

[10] Clark, E. B. and B. Roebuck. Extending the application areas for titanium carbonitride cermets. *International Journal of Refractory Metals and Hard Materials*, Vol. 11, 1992, pp. 23–33.

[11] Sulima, I. Tribological properties of steel/TiB₂ composites prepared by spark plasma sintering. *Archives of Metallurgy and Materials*, Vol. 59, 2014, pp. 1263–1268.

[12] Munro, R. G. Material properties of titanium diboride. *Journal of Research of the National institute of standards and Technology*, Vol. 105, 2000, pp. 709–720.

[13] Zhao, X. R., D. W. Zuo, M. X. Zhang, F. Xu, and S. S. Feng. In situ production of ultra-fine Ti(C,N)-TiB2-Co cermets by reactive hot processing from the Co-Ti-C-BN system. *International Journal of Refractory Metals and Hard Materials*, Vol. 55, 2016, pp. 1–10.

[14] Zhang, G. J., Z. Z. Jin, and X. M. Yue. TiB2-Ti(C,N)-SiC composites prepared by reactive hot pressing. *Journal of Materials Science Letters*, Vol. 15, 1996, pp. 26–28.

[15] Shankar, E., S. B. Prabu, and K. A. Padmanabhan. Mechanical properties and microstructures of TiCN/nano-TiB2/TiN cermets prepared by spark plasma sintering. *Ceramics International*, Vol. 44, 2018, pp. 9384–9394.

[16] Shimada, S., A. Takahashi, H. Kiyono, and J. Tsujino. Coatings and microstructures of monolithic TiB2 films and double layer and composite TiCN/TiB2 films from alkoxide solutions by thermal plasma CVD. *Thin Solid Films*, Vol. 516, 2008, pp. 6616–6621.

[17] Bahce, E. and N. Cakir. Tribological investigation of multilayer CrN/CrCN/TaN films deposited by close field unbalanced magnetron sputtering. *Reviews on Advanced Materials Science*, Vol. 58, 2019, pp. 271–279.

[18] Wolfe, D. E. and J. Singh. Synthesis and characterization of TiBCN coatings deposited by ion beam assisted, co-evaporation electron beam-physical vapor deposition (EB-PVD). *Journal of Materials Science*, Vol. 37, 2002, pp. 3777–3787.

[19] Ferrari, A. C. and J. Robertson. Resonant Raman spectroscopy of disordered, amorphous, and diamondlike carbon. *Physical Review B*, Vol. 64, 2000, id. 075414.

[20] Gilkes, K. W. R., S. Prawer, K. W. Nugent, J. Robertson, H. S. Sands, Y. Lifshitz, et al. Direct quantitative detection of the sp³ bonding in diamond-like carbon films using ultraviolet and visible Raman spectroscopy. *Journal of Applied Physics*, Vol. 87, 2000, pp. 7283–7289.

[21] Oshiro, T., M. Yamazato, A. Higa, and M. Toguchi. Raman analysis of trans-polyacetylene chains in hydrogenated amorphous carbon films. *Japanese Journal of Applied Physics*, Vol. 46, 2007, id. 756.

[22] O., Knotek, R., Breidenbach, F., Jungblut, et al. Ti-B-C-N coatings. *Surface and Coatings Technology*, Vol. 43, 1990, pp. 107–115.

[23] Aliyu, A. and C. Srivastava. Correlation between growth texture, crystallite size, lattice strain and corrosion behavior of copper-carbon nanotubes composite coatings. *Surface and Coatings Technology*, Vol. 405, 2021, id. 126596.

[24] Wagner, C. D., J. F. Moulder, L. E. Davis, and W. M. Riggs. Physical electronics. *Handbook of X-ray photoelectron spectroscopy*, Vol. 20, Perkin–Elmer Corporation, 1979.

[25] Zeng, Q. and Z. Ning. High-temperature tribological properties of diamond-like carbon films: A review. *Reviews on Advanced Materials Science*, Eden Prairie, Minnesota, USA, Vol. 60, 2021, pp. 276–292.